Geophysical Research Letters

RESEARCH LETTER
10.1029/2018GL080397

The Rupture Process of the 2018 M_w 6.9 Hawai'i Earthquake as Imaged by a Genetic Algorithm-Based Back-Projection Technique

H. L. Kehoe[1], E. D. Kiser[1], and P. G. Okubo[2]

[1]Department of Geosciences, University of Arizona, Tucson, AZ, USA, [2]Hawaiian Volcano Observatory, U.S. Geological Survey, Hawaii National Park, HI, USA

Key Points:
- The complex rupture process of the 2018 M_w 6.9 Hawai'i earthquake is imaged using a genetic algorithm-based back-projection technique
- The dominant high-frequency feature of this earthquake is a slow western propagating rupture that overlaps with previous slow slip events
- These rupture properties can be explained by slip on a décollement composed of soft sediments with small velocity-weakening asperities

Supporting Information:
- Supporting Information S1
- Movie S1
- Data Set S1
- Figure S1
- Figure S2
- Figure S3
- Figure S4
- Figure S5
- Figure S6
- Figure S7

Correspondence to:
H. L. Kehoe,
hlkehoe@email.arizona.edu

Citation:
Kehoe, H. L., Kiser, E. D., & Okubo, P. G. (2019). The rupture process of the 2018 M_w 6.9 Hawai'i earthquake as imaged by a genetic algorithm-based back-projection technique. *Geophysical Research Letters*, *46*, 2467–2474. https://doi.org/10.1029/2018GL080397

Received 7 SEP 2018
Accepted 30 JAN 2019
Accepted article online 6 FEB 2019
Published online 7 MAR 2019

Abstract An episode of unrest began at Kīlauea in April 2018 that produced both significant volcanic output and high rates of seismicity, including a M_w 6.9 earthquake on 4 May 2018. In this study, we image the rupture process of this earthquake using a genetic algorithm-based back-projection technique. The dominant feature of the earthquake is a slowly propagating western rupture, which shares similar characteristics with the region's largest recorded event in 1975 (M_w 7.7). The location of this western segment suggests that small asperities on this section of the décollement that frequently fail as slow slip events may achieve seismic slip rates when rupture is initiated on adjacent sections of the fault. Given the interaction between volcanic and seismic activity in this region, imaging the rupture properties of these events can improve our understanding of future geologic hazards in this region.

Plain Language Summary Voluminous lava flows and explosive eruptions at Kīlauea Volcano in Hawai'i have captured the attention of the media and general public during the past year. In the early stages of this volcanic activity, a magnitude 6.9 earthquake occurred beneath the south flank of Kīlauea, which was the second largest earthquake recorded by modern instrumentation in this region. The research presented in the manuscript uses a novel source imaging technique to study the fine-scale spatiotemporal evolution of the rupture that produced this event. The details of this rupture provide new insight into the relationship between fault properties, background seismicity, slow slip events, and major earthquakes in volcanic settings.

1. Introduction

Since 1983, nearly continuous volcanic activity within the East Rift Zone (ERZ), known as the Pu'u 'Ō'ō eruption, has produced large quantities of lava that has remade the landscape of eastern Hawai'i. On 3 May 2018, a new episode of lava output began in the lower ERZ located near the eastern corner of Hawai'i. Twenty-four separate fissures formed during this activity, and as of 9 August 2018, 35.5 km^2 of land has been affected by the resulting lava flows (Neal et al., 2019). This activity is also associated with several minor explosive eruptions from the Kīlauea summit, which generated earthquakes with moment magnitudes as large as 5.4 (U.S. Geological Survey National Earthquake Information Center [NEIC]: https://earthquake.usgs.gov/earthquakes/eventpage/hv70219637/executive). Several earthquakes also occurred along the ERZ associated with the movement of magma in the subsurface. Away from both the summit and ERZ, the largest earthquake during this episode (M_w 6.9) occurred on 4 May 2018 beneath the south flank of Kīlauea (22:32:54 UTC, 19.318°N 155.000°W, depth 5.8 km; NEIC: https://earthquake.usgs.gov/earthquakes/eventpage/us1000dyad/executive).

The hypocenter of this earthquake is similar to other large (M_w > 6.0) events that have occurred in this region, and it has been argued that slip during these events takes place on the décollement (7- to 13-km depth) that separates the overlying volcanic edifice of Kīlauea from the underlying oceanic crust (Crosson & Endo, 1982; Denlinger & Okubo, 1995). This low-angle décollement dips northwest toward the center of the Hawai'i Island and likely extends southeast 30–50 km offshore to a topographic bench (Denlinger & Okubo, 1995). Several studies have concluded that motion on the décollement is driven by injection of magma into the East and Southwest Rift Zones (Denlinger & Okubo, 1995; Dvorak et al., 1986; Swanson et al., 1976), though gravitational forces may also be important (Denlinger & Morgan, 2014). The 1975 M_w 7.7 Kalapana earthquake was the largest earthquake on the décollement recorded

by modern instruments (Nettles & Ekström, 2004). Events of this magnitude can significantly change the stress state of the Kīlauea magmatic system, and it is thought that increased extensional stresses in the ERZ associated with the 1975 earthquake resulted in a prolonged period of reduced volcanic output (Cayol et al., 2000; Denlinger & Morgan, 2014). In addition to abundant seismicity on sections of the décollement, this surface also hosts aseismic creep (Owen et al., 2000) and slow slip events (Brooks et al., 2006; Foster et al., 2013; Montgomery-Brown et al., 2009, 2013; Poland et al., 2010; Segall et al., 2006; Syracuse et al., 2010). These slow slip events have equivalent magnitudes between 5.3 and 6.0 (Montgomery-Brown et al., 2013) and occur off the southern coast of Kīlauea where little seismicity is typically observed.

The NEIC hypocenter and the global centroid-moment-tensor focal mechanism (Ekström et al., 2012) of the 2018 M_w 6.9 earthquake suggest that this earthquake occurred on the low-angle décollement (Figure 1). In this study, the rupture properties of this event are investigated using the back-projection method, which time shifts and stacks waveforms recorded at teleseismic distances to a grid of potential source locations to determine where seismic sources are located as a function of time (Ishii et al., 2005; Krüger & Ohrnberger, 2005). From this information, rupture properties such as rupture area, direction, and speed can be estimated. This method was originally used with seismic arrays (Ishii et al., 2005, 2007; Krüger & Ohrnberger, 2005), though several studies have also applied the method to a larger (e.g., global) distribution of seismic stations (Walker et al., 2005). This global approach can significantly improve resolution but can also hinder the coherence of waveforms due to complexities in the source and structure of the Earth, leading to artifacts in the back-projection results. The current study uses a novel genetic algorithm selection scheme to determine the seismic stations that should be used to reduce artifacts that arise from using a large distribution of seismic stations (Text S2 in the supporting information). The key idea behind this algorithm is that waveforms from seismic stations should be chosen such that they image small earthquakes as point sources. This method is applied to seismic stations around the northern circum-Pacific including stations in the Transportable Array in Alaska and the High Sensitivity Seismographic Network (Hi-net) in Japan (Figure 2). Seismic stations in the Southern Hemisphere are excluded from the analysis due to their sparse distribution at teleseismic distances and the limited theoretical resolution improvement that they would provide (Figure S7).

2. Methods

The back-projection method (Ishii et al., 2005) can be used with any network of seismic stations and any seismic phase, though *P* waves recorded at teleseismic distances are most often used because there is limited interference with other seismic phases for most earthquakes. The method is typically used with seismic arrays that have small station spacing and limited overall aperture. For these cases, the paths of waves from the source to the receivers are similar, which produces coherent recorded waveforms across the array. The coherence of the waveforms enhances the stacking process and efficiently removes artifacts from the source image. Though the use of a single array typically produces robust results, the limited aperture also limits both spatial and temporal resolution. An increased distribution of seismic stations can be used to improve resolution, though care must be taken to avoid source image artifacts produced by incoherent data. This is typically done by either visual inspection of the data or using a measure of the similarity between portions of the waveforms (e.g., correlation value). Though selecting data based upon the characteristics of the waveforms can be useful, this approach does not directly address the source of artifacts in the back-projection results.

In this study, *P* waves from a broad distribution of northern circum-Pacific teleseismic stations are used to image the rupture properties of the 2018 M_w 6.9 Hawai'i earthquake. These stations include the Transportable Array in Alaska, several networks in the contiguous United States, and Hi-net in Japan. The *P* waves from a small earthquake near the hypocenter of the mainshock are aligned using a cross-correlation procedure (Ishii et al., 2007). This step makes empirical travel time corrections to the data such that the arrival times of *P* waves are the same as those calculated using a one-dimensional Earth model, iasp91 (Kennett & Engdahl, 1991). This step also normalizes *P* wave amplitudes and corrects waveform polarities such that the initial waveforms have the same polarity. Several previous studies have developed methods for designing arrays that optimize resolution (e.g., Rost & Thomas, 2002) and reduce the effects

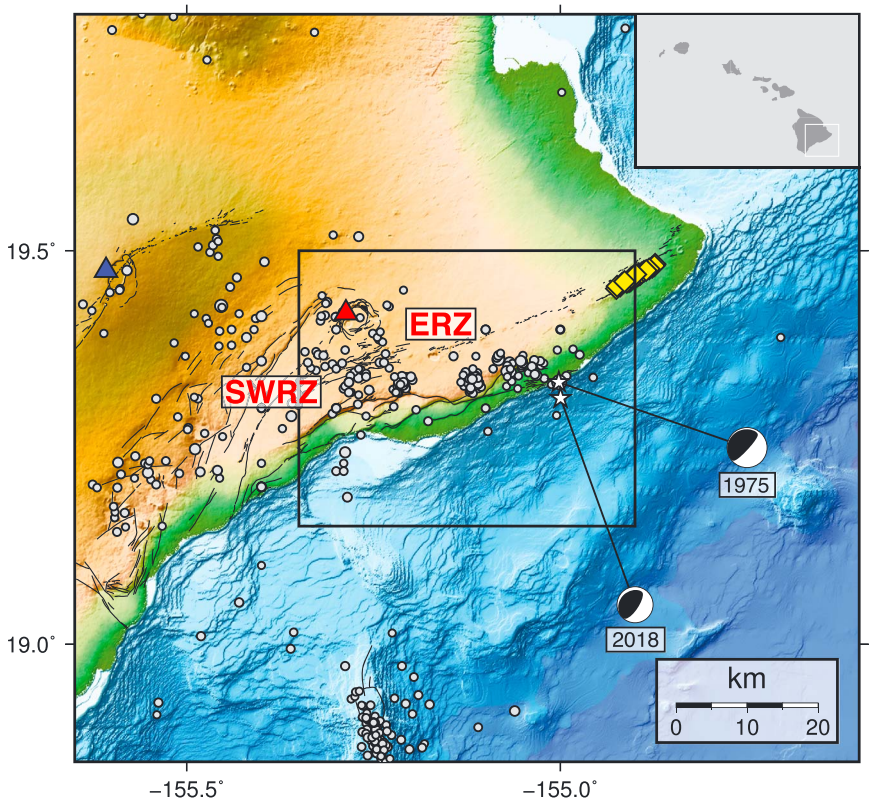

Figure 1. Geographic map of Hawai'i. The 2018 M_w 6.9 and 1975 M_w 7.7 National Earthquake Information Center epicenters are indicated by the 2018 and 1975 centroid-moment-tensor focal mechanisms, respectively. The red triangle is the location of the Kīlauea summit. The red ERZ and SWRZ labels show the locations of the East and Southwest Rift Zones, respectively. The blue triangle is the location of the Mauna Loa summit. The yellow diamonds are the locations of fissures. The black lines are faults. The magnitude-scaled gray dots show historical seismicity above magnitude 4.0 from 1955 to present (National Earthquake Information Center). The black box outlines the study area in Figure 3. The inset shows the location of the map on the state of Hawaii.

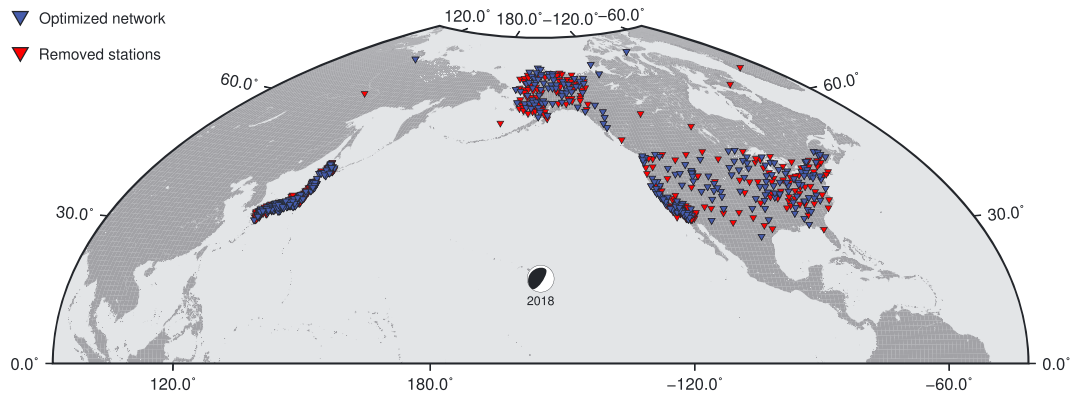

Figure 2. Distribution of stations. The inverted triangles are the locations of the 805 stations used in this study. The red inverted triangles are the 375 stations removed by the genetic algorithm and the blue inverted triangles are the 430 stations kept by the genetic algorithm (optimized network). The centroid-moment-tensor focal mechanism represents the 2018 M_w 6.9 mainshock. Figure S5 shows detailed station distributions in Japan, Alaska, and the continental United States.

of noisy data on array processing techniques (Goldstein & Archuleta, 1987; Meng et al., 2011; Schmidt, 1986). In this work, a genetic algorithm (e.g., Gallagher & Sambridge, 1994; Holland, 1992; Sambridge & Mosegaard, 2002) is used to determine a subset of the northern circum-Pacific stations that best image small earthquakes (magnitudes 4.6–5.4) in the mainshock area as point sources (Text S2 and Figures S3–S6). This approach is designed to simultaneously remove stations with misaligned or noisy data, select a distribution of stations that produces good theoretical array resolution, and select a distribution of stations that reduces the effects of unwanted seismic phases that can produce high-amplitude stacks at incorrect locations and times. Using this optimal array, mainshock waveforms are aligned separately and back projected using a coherence-based approach (Ishii, 2011) to determine the spatiotemporal source properties of the event. In order to estimate the relative source-time function of the mainshock, a separate linear stacking back-projection analysis is performed and the largest amplitude value for all grid points at each time step is plotted as a function of time.

3. Data

Seismic data was retrieved from the Incorporated Research Institutions for Seismology Consortium and the National Research Institute for Earth Science and Disaster Resilience in Japan. The alignment event used to determine empirical time corrections for the back-projection analysis occurred on 3 May 2018 and had a body wave magnitude of 5.1 (20:30:56 UTC, 19.344°N 155.070°W, 6.9-km depth; NEIC: https://earthquake.usgs.gov/earthquakes/eventpage/us1000dxhr/executive). The hypocenter of this event is 8.4 km from the mainshock hypocenter. The point source events used for the genetic algorithm-based network optimization occurred on 4 May 2018 (21:32:44 UTC, 19.342°N 155.032°W, 6.9-km depth; NEIC: https://earthquake.usgs.gov/earthquakes/eventpage/us1000dy8n/executive) and 5 May 2018 (03:30:15, 19.069°N 155.046°W, 8.7-km depth; NEIC: https://earthquake.usgs.gov/earthquakes/eventpage/hv70117676/executive). The moment magnitude of the first event was 5.4, and the short-period body wave magnitude of the second event was 4.6. The first event was 20.7 km from the mainshock hypocenter and the second event was 27.5 km from the mainshock hypocenter. Figure S3 shows how the fitness value of the point source events increases as a function of generation number of the genetic algorithm, and Figure S4 shows the source image improvement of the point source events from the full network to the optimal network. All data used are band-pass filtered to a frequency range of 0.8–2.0 Hz.

4. Results

The back-projection analysis images four distinct rupture directions associated with the 2018 M_w 6.9 earthquake (Figure 3a). The rupture initiates near the reported hypocenter and propagates north at ~1.5 km/s (Segment 1). At 4 s after the hypocentral time, the imaged rupture transitions to a northwest propagation direction with a speed of ~2.3 km/s (Segment 2). The next segment propagates south at an anomalously high rupture speed of ~4.3 km/s (Segment 3). The final imaged segment of the rupture occurs offshore and propagates west at ~0.7 km/s (Segment 4). The westward propagation associated with Segment 4 can be seen in the Incorporated Research Institutions for Seismology back-projection results (https://doi.org/10.17611/DP/16504384). The time evolution of energy release is determined by plotting the largest amplitude value for all grid points at each time step in the linear back-projection result (Figure 3b). The amplitude of high-frequency energy release is highest during Segment 4. The total duration of this earthquake is estimated to be 33 s. Following the west propagating rupture, there is an imaged episode of high-frequency energy release slightly south of the Kīlauea summit, though the spatial separation between this feature and the mainshock rupture indicates that it is either an early aftershock or an artifact (Movie S1). The rupture area of the mainshock, as estimated by summing the area within the 0.925 contour of the normalized source image at each time step of the event, is approximately 200 km^2, and the rupture lengths of Segments 1–4 are approximately 4.4, 4.6, 9.6, and 9.5 km, respectively. The 0.925 contour is used because the estimated rupture area significantly increases at normalized amplitude contours lower than this value, likely due to the background noise in the back-projection result. The slow overall rupture speed and long duration of this event are consistent with previous studies of this earthquake (Bai et al., 2018; Liu et al., 2018).

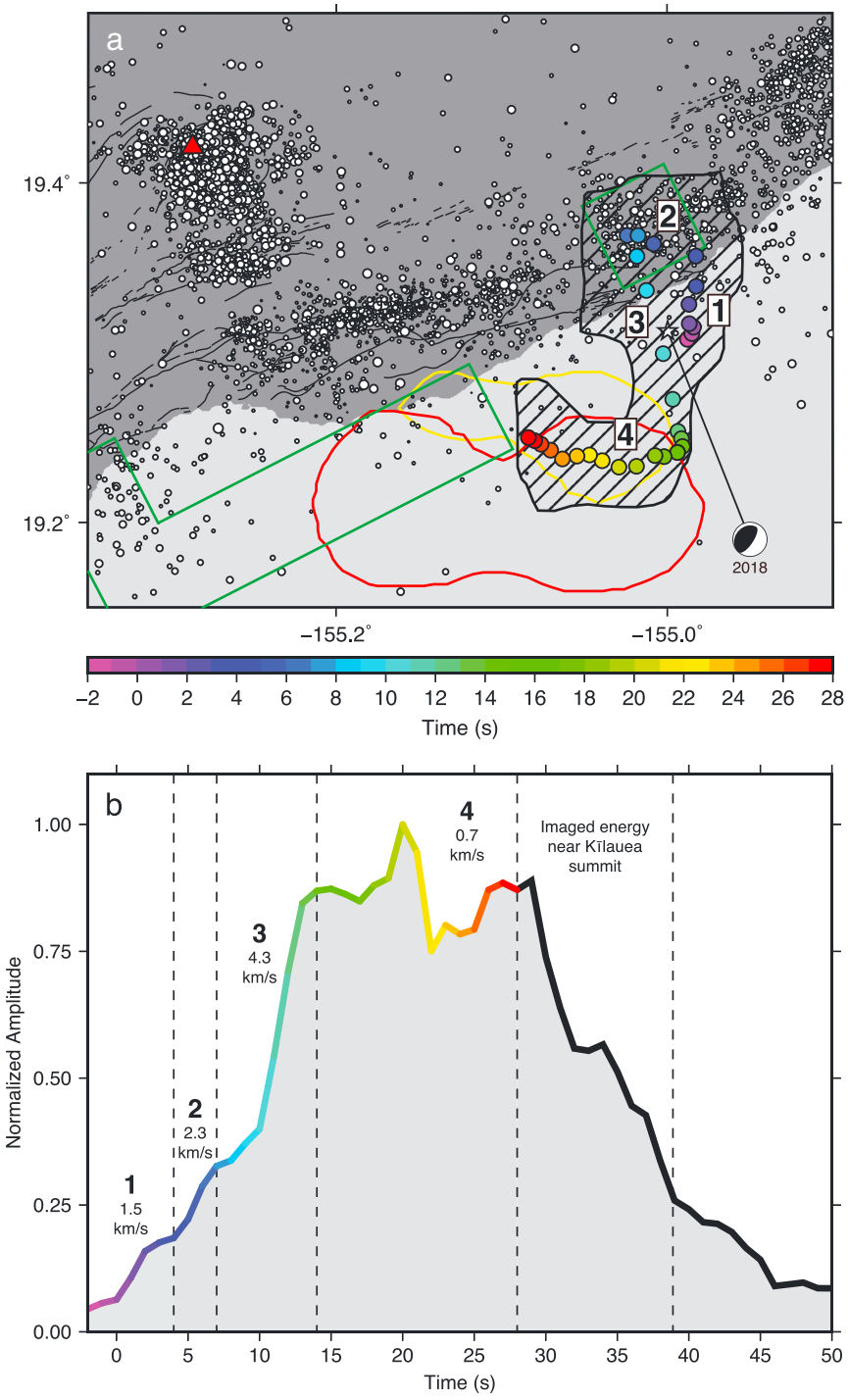

Figure 3. Summary of results. (a) The rainbow dots, determined from the coherence-based back-projection result, show the central source locations of the 2018 M_w 6.9 earthquake (Data Set S1). The color of the dots indicates rupture time with respect to the hypocentral time (0 s). The individual segments of the overall rupture are labeled in white boxes. The white star is the National Earthquake Information Center epicenter, and black hatched area shows the estimated rupture area of the imaged earthquake. The red and yellow lines show the locations of periodic and aperiodic slow slip events, respectively (Foster et al., 2013). The green boxes show the distribution of largest slip (greater than 10 m) from the 1975 M_w 7.7 event (Owen & Bürgmann, 2006). The magnitude-scaled white dots show the post-mainshock seismicity located by Hawaiian Volcano Observatory (https://doi.org/10.7914/SN/HV). The black lines are faults. The dark and light gray background areas show onshore and offshore regions, respectively. (b) The normalized amplitude of high-frequency energy release as a function of time, determined from the linear back-projection result, is shown for the 2018 M_w 6.9 earthquake. The rainbow line of the source time function corresponds to the rainbow dots used in (a). The western rupture (Segment 4) shows the highest normalized amplitude.

5. Discussion and Conclusions

The back-projection analysis images significant complexity in both the directions and speeds of the individual segments that compose this rupture. Though the rupture direction changes between Segments 1 and 2, these features represent continuous propagation at speeds that are typical given local seismic wave velocities in this region (Lin et al., 2014; Syracuse et al., 2010). Assuming these segments involve slip on the décollement, they occur on a section of this fault where background seismicity is common (Figure 3a). In contrast to this typical rupture behavior, a particularly anomalous feature is the high speed of Segment 3 that connects the onshore and offshore components of the rupture (Segments 2 and 4). The high rupture speed calculated for Segment 3 likely indicates a noncontinuous rupture that can be explained in one of the two following ways. First, synthetic results indicate that this feature may represent a spatial jump in the location of slip along the décollement between Segments 2 and 4 (Figure S1). The spatiotemporal gap between these segments would suggest either static or dynamic stress triggering as the cause of this jump. The second possibility is that Segment 1 includes a southern rupture with amplitudes too low to be imaged in the back-projection results (Figure S2). In this scenario, the hypothetical southern rupture connects the beginning of Segment 1 with Segment 4 without any spatial gaps in the overall rupture.

The fourth segment of the rupture is the dominant feature of this earthquake in terms of both the amplitude of energy release and the propagation length (Figure 3). This segment occurs 5–10 km offshore where both background seismicity and aftershocks are sparse (Figure 3a). In addition, this region of the décollement experiences slow slip events (Brooks et al., 2006; Foster et al., 2013; Montgomery-Brown et al., 2009, 2013; Poland et al., 2010; Segall et al., 2006; Syracuse et al., 2010). Modeling results have shown that the failure of velocity-weakening patches with dimensions close to the critical nucleation dimension can produce these slow slip events (Kato, 2004). Small velocity-weakening patches are also thought to produce high-frequency radiation during large earthquakes (e.g., Lay et al., 2012). Given that seismic slip rates initiated on an adjacent section of the décollement during the 2018 M_w 6.9 mainshock, the overlap between the area of slow slip events and the segment of rupture that produced the highest-amplitude high-frequency seismic waves (Segment 4) indicates that this section of the décollement may be composed of small velocity-weakening patches embedded within a larger region of stable sliding. The location of Segment 4 would also suggest that stress accumulation on the décollement is not completely relieved by the slow slip events. The path of Segment 4 is near the boundary between patches of periodic and aperiodic slow slip behavior (Foster et al., 2013). If this boundary region represents a zone of reduced slow slip between the northern and southern slow slip patches (Figure 3a), then one would expect a high rate of stress accumulation in the absence of stable sliding, possibly explaining the propagation of this rupture into this region.

Several studies have concluded that the 1975 M_w 7.7 event had an anomalously long duration and ruptured west/southwest from its epicenter, which is ~4 km from the 2018 M_w 6.9 epicenter (Harvey & Wyss, 1986; Ma et al., 1999; Owen & Bürgmann, 2006). The detailed rupture properties of the 1975 event have been debated due to data limitations at the time, though recent studies of this event have argued that significant slip occurred offshore (Ma et al., 1999; Nettles & Ekström, 2004; Owen & Bürgmann, 2006). The 1975 and 2018 ruptures exhibit little overlap but fill the majority of the total décollement area (Figure 3a). There are also several similarities between the dynamic properties of these events. Both events had long durations given their magnitudes and low estimated rupture velocities (Harvey & Wyss, 1986), though this latter point only applies to Segment 4 for the 2018 mainshock. Both events also seem to have initiated near the coast where seismicity is abundant and then propagated offshore. In both cases, this offshore rupture is not associated with a spatially correlated aftershock sequence. These characteristics of the 1975 and 2018 earthquakes are similar to those observed for large events at near-trench locations of subduction zones. In the subduction zone setting, this seismic behavior is explained by soft sediments that compose the subduction interface in near-trench environments (Kanamori & Kikuchi, 1993). The low seismic velocities and anelasticity of this material lead to slow rupture speeds and an inefficient transfer of stress that limits aftershock sequences. A similar argument may be applicable to the sediments that form the décollement between the volcanic edifice of Kīlauea and the underlying oceanic crust. Near-trench subduction zone earthquakes differ in frequency content from the 1975 Kalapana and 2018 Hawai'i events, which generated significant high-frequency seismic radiation (Harvey & Wyss, 1986). This high-frequency radiation may be caused by the failure of small velocity-weakening patches

embedded within an area of stable sliding (i.e., the soft sediments of the décollement). Given that the heterogeneous frictional properties of this interface provide the potential for both strong ground shaking and the generation of tsunami waves during large earthquakes, an improved understanding of the regions of the décollement that may experience significant slip during future large-magnitude events is critical for evaluating hazards in this region.

Acknowledgments
The authors acknowledge the Incorporated Research Institutions for Seismology (IRIS) Consortium and the National Research Institute for Earth Science and Disaster Resilience (NIED) in Japan for making digital seismic data open and readily available. The authors also acknowledge the Hawaiian Volcano Observatory (HVO) for access to their earthquake catalog. The Generic Mapping Tools (GMT) were used to create figures presented in this manuscript. Constructive comments and suggestions from Miaki Ishii, Gavin Hayes, Weston Thelen, and one anonymous reviewer have helped improve the results presented in this manuscript. The back-projection results are available in the supporting information.

References

Bai, Y., Ye, L., Yamazaki, Y., Lay, T., & Cheung, K. F. (2018). The 4 May 2018 M_w 6.9 Hawaii Island earthquake and implications for tsunami hazards. *Geophysical Research Letters*, *45*, 11,040–11,049. https://doi.org/10.1029/2018GL079742

Brooks, B. A., Foster, J. H., Bevis, M., Frazer, L. N., Wolfe, C. J., & Behn, M. (2006). Periodic slow earthquakes on the flank of Kīlauea volcano, Hawai'i. *Earth and Planetary Science Letters*, *246*, 207–216. https://doi.org/10.1016/j.epsl.2006.03.035

Cayol, V., Dieterich, J. H., Okamura, A. T., & Miklius, A. (2000). High magma storage rates before the 1983 eruption of Kilauea, Hawaii. *Science*, *288*(5475), 2343–2346. https://doi.org/10.1126/science.288.5475.2343

Crosson, R. S., & Endo, E. T. (1982). Focal mechanisms and locations of earthquakes in the vicinity of the 1975 Kalapana earthquake aftershock zone 1970–1979: Implications for tectonics of the south flank of Kilauea Volcano, island of Hawaii. *Tectonics*, *1*(6), 495–542. https://doi.org/10.1029/TC001i006p00495

Denlinger, R. P., & Morgan, J. K. (2014). Instability of Hawaiian volcanoes. In *Characteristics of Hawaiian volcanoes* (Vol. 1801, Chap. 4, pp. 149–176). US Geological Survey Professional Paper. https://doi.org/10.3133/pp1801

Denlinger, R. P., & Okubo, P. G. (1995). Structure of the mobile south flank of Kilauea Volcano, Hawaii. *Journal of Geophysical Research*, *100*(B12), 24,499–24,507. https://doi.org/10.1029/95JB01479

Dvorak, J. J., Okamura, A. T., English, T. T., Koyanagi, R. Y., Nakata, J. S., Sako, M. K., et al. (1986). Mechanical response of the south flank of Kilauea Volcano, Hawaii, to intrusive events along the rift systems. *Tectonophysics*, *124*(3–4), 193–209. https://doi.org/10.1016/0040-1951(86)90200-3

Ekström, G., Nettles, M., & Dziewoński, A. M. (2012). The global CMT project 2004–2010: Centroid-moment tensors for 13,017 earthquakes. *Physics of the Earth and Planetary Interiors*, *200-201*, 1–9. https://doi.org/10.1016/J.PEPI.2012.04.002

Foster, J. H., Lowry, A. R., & Brooks, B. A. (2013). Fault frictional parameters and material properties revealed by slow slip events at Kilauea volcano, Hawai'i. *Geophysical Research Letters*, *40*, 6059–6063. https://doi.org/10.1002/2013GL058234

Gallagher, K., & Sambridge, M. (1994). Genetic algorithms: A powerful tool for large-scale nonlinear optimization problems. *Computers & Geosciences*, *20*(7–8), 1229–1236. https://doi.org/10.1016/0098-3004(94)90072-8

Goldstein, P., & Archuleta, R. J. (1987). Array analysis of seismic signals. *Geophysical Research Letters*, *14*(1), 13–16. https://doi.org/10.1029/GL014i001p00013

Harvey, D., & Wyss, M. (1986). Comparison of a complex rupture model with the precursor asperities of the 1975 Hawaii *Ms* = 7.2 earthquake. *Pure and Applied Geophysics*, *124*(4–5), 957–973. https://doi.org/10.1007/BF00879621

Holland, J. H. (1992). *Adaptation in natural and artificial systems: An introductory analysis with applications to biology, control, and artificial intelligence*. MIT press. https://doi.org/10.7551/mitpress/1090.001.0001

Ishii, M. (2011). High-frequency rupture properties of the M_w 9.0 off the Pacific coast of Tohoku earthquake. *Earth, Planets and Space*, *63*, 609–614. https://doi.org/10.5047/eps.2011.07.009

Ishii, M., Shearer, P. M., Houston, H., & Vidale, J. E. (2005). Extent, duration and speed of the 2004 Sumatra-Andaman earthquake imaged by the Hi-Net array. *Nature*, *435*, 933–936. https://doi.org/10.1038/nature03675

Ishii, M., Shearer, P. M., Houston, H., & Vidale, J. E. (2007). Teleseismic *P* wave imaging of the 26 December 2004 Sumatra-Andaman and 28 March 2005 Sumatra earthquake ruptures using the Hi-net array. *Journal of Geophysical Research*, *112*, B11307. https://doi.org/10.1029/2006JB004700

Kanamori, H., & Kikuchi, M. (1993). The 1992 Nicaragua earthquake: A slow tsunami earthquake associated with subducted sediments. *Nature*, *361*(6414), 714–716. https://doi.org/10.1038/361714a0

Kato, N. (2004). Interaction of slip on asperities: Numerical simulation of seismic cycles on a two-dimensional planar fault with nonuniform frictional property. *Journal of Geophysical Research*, *109*, 1–17. https://doi.org/10.1029/2004JB003001

Kennett, B. L. N., & Engdahl, E. R. (1991). Traveltimes for global earthquake location and phase identification. *Geophysical Journal International*, *105*(2), 429–465. https://doi.org/10.1111/j.1365-246X.1991.tb06724.x

Krüger, F., & Ohrnberger, M. (2005). Tracking the rupture of the M_w = 9.3 Sumatra earthquake over 1,150 km at teleseismic distance. *Nature*, *435*, 937–939. https://doi.org/10.1038/nature03696

Lay, T., Kanamori, H., Ammon, C. J., Koper, K. D., Hutko, A. R., Ye, L., et al. (2012). Depth-varying rupture properties of subduction zone megathrust faults. *Journal of Geophysical Research*, *117*, B04311. https://doi.org/10.1029/2011JB009133

Lin, G., Shearer, P. M., Matoza, R. S., Okubo, P. G., & Amelung, F. (2014). Three-dimensional seismic velocity structure of Mauna Loa and Kilauea volcanoes in Hawaii from local seismic tomography. *Journal of Geophysical Research: Solid Earth*, *119*, 4377–4392. https://doi.org/10.1002/2013JB010820.We

Liu, C., Lay, T., & Xiong, X. (2018). Rupture in the 4 May 2018 M_w 6.9 earthquake seaward of the Kilauea East Rift Zone fissure eruption in Hawaii. *Geophysical Research Letters*, *45*, 9508–9515. https://doi.org/10.1029/2018GL079349

Ma, K.-F., Kanamori, H., & Satake, K. (1999). Mechanism of the 1975 Kalapana, Hawaii, earthquake inferred from tsunami data. *Journal of Geophysical Research*, *104*(B6), 13,153–13,167. https://doi.org/10.1029/1999JB900073

Meng, L., Inbal, A., & Ampuero, J.-P. (2011). A window into the complexity of the dynamic rupture of the 2011 M_w 9 Tohoku-Oki earthquake. *Geophysical Research Letters*, *38*, L00G07. https://doi.org/10.1029/2011GL048118

Montgomery-Brown, E. K., Segall, P., & Miklius, A. (2009). Kilauea slow slip events: Identification, source inversions, and relation to seismicity. *Journal of Geophysical Research*, *114*, B00A03. https://doi.org/10.1029/2008JB006074

Montgomery-Brown, E. K., Thurber, C. H., Wolfe, C. J., & Okubo, P. G. (2013). Slow slip and tremor search at Kilauea Volcano, Hawaii. *Geochemistry, Geophysics, Geosystems*, *14*, 367–384. https://doi.org/10.1002/ggge.20044

Neal, C. A., Brantley, S. R., Antolik, L., Babb, J. L., Burgess, M., Calles, K., et al. (2019). The 2018 rift eruption and summit collapse of Kīlauea Volcano. *Science (New York, N.Y.)*, *363*(6425), 367–374. https://doi.org/10.1126/science.aav7046

Nettles, M., & Ekström, G. (2004). Long-period source characteristics of the 1975 Kalapana, Hawaii, earthquake. *Bulletin of the Seismological Society of America*, *94*, 422–429. https://doi.org/10.1785/0120030090

Owen, S. E., & Bürgmann, R. (2006). An increment of volcano collapse: Kinematics of the 1975 Kalapana, Hawaii, earthquake. *Journal of Volcanology and Geothermal Research*, *150*, 163–185. https://doi.org/10.1016/j.jvolgeores.2005.07.012

Owen, S. E., Segall, P., Lisowski, M., Miklius, A., Denlinger, R. P., & Sako, M. K. (2000). Rapid deformation of Kilauea Volcano: Global Positioning System measurements between 1990 and 1996. *Journal of Geophysical Research*, *105*(B8), 18,983–18,998. https://doi.org/10.1029/2000JB900109

Poland, M. P., Miklius, A., Wilson, D., & Okubo, P. G. (2010). Slow slip event at Kīlauea Volcano. *Eos*, *34*, 118–119. https://doi.org/10.1029/2007GL031625

Rost, S., & Thomas, C. (2002). Array seismology: Methods and applications. *Reviews of Geophysics*, *40*(3), 1008. https://doi.org/10.1029/2000RG000100

Sambridge, M., & Mosegaard, K. (2002). Monte Carlo methods in geophysical inverse problems. *Reviews of Geophysics*, *40*(3), 1009. https://doi.org/10.1029/2000RG000089

Schmidt, R. (1986). Multiple emitter location and signal parameter estimation. *IEEE Transactions on Antennas and Propagation*, *34*(3), 276–280. https://doi.org/10.1109/TAP.1986.1143830

Segall, P., Desmarais, E. K., Shelly, D., Miklius, A., & Cervelli, P. (2006). Earthquakes triggered by silent slip events on Kīlauea volcano, Hawaii. *Nature*, *442*(7098), 71–74. https://doi.org/10.1038/nature04938

Swanson, D. A., Duffield, W. A., & Fiske, R. S. (1976). Displacement of the south flank of Kilauea volcano; The result of forceful intrusion of magma into the rift zones. Professional Paper. Retrieved from http://pubs.er.usgs.gov/publication/pp963

Syracuse, E. M., Thurber, C. H., Wolfe, C. J., Okubo, P. G., Foster, J. H., & Brooks, B. A. (2010). High-resolution locations of triggered earthquakes and tomographic imaging of Kilauea Volcano's south flank. *Journal of Geophysical Research*, *115*, B10310. https://doi.org/10.1029/2010JB007554

Walker, K. T., Ishii, M., & Shearer, P. M. (2005). Rupture details of the 28 March 2005 Sumatra M_w 8.6 earthquake imaged with teleseismic *P* waves. *Geophysical Research Letters*, *32*, L24303. https://doi.org/10.1029/2005GL024395